Research Article | Vol. 28, No. 26 / 21 December 2020 / Optics Express 38579
Optics EXPRESS

Back-side-on-BOX heterogeneously integrated III-V-on-silicon O-band discrete-mode lasers

TORREY THIESSEN,[1,*] SYLVIE MENEZO,[2] CHRISTOPHE JANY,[3] JASON C. C. MAK,[1] AND JOYCE K. S. POON[1,4]

[1]Department of Electrical and Computer Engineering, University of Toronto, 10 King's College Road, Toronto, Ontario M5S 3G4, Canada
[2]SCINTIL Photonics, 38040 Grenoble Cedex, France
[3]CEA-Leti, 17 rue des Martyrs, 38000 Grenoble, France
[4]Max Planck Institute of Microstructure Physics, Weinberg 2, 06120 Halle, Germany
[*]torrey.thiessen@mail.utoronto.ca

Abstract: We demonstrate foundry-fabricated O-band III-V-on-silicon discrete-mode lasers. The laser fabrication follows the back-side-on-buried-oxide laser integration process and is compatible with complex, multilayer, silicon-on-insulator based platforms. A series of devices were characterized, with the best devices producing on-chip powers of nearly 20 mW with Lorentzian linewidths below 20 kHz and a side mode suppression ratio of at least 60 dB.

1. Introduction

The advantages of semiconductor lasers is their small size, low cost, and mass manufacturability make them ideally suited to applications requiring dense integration. Until recently, however, a drawback of semiconductor lasers is their relatively high noise (linewidths ≥100 kHz) compared to what can be achieved in fiber and solid-state lasers. Many applications can benefit from low-noise semiconductor lasers, including coherent data transmission with advanced modulation formats [1–3], optical frequency synthesis [4], microwave photonics [5], high performance sensing [6,7], and LiDAR [8].

Achieving narrow linewidth laser diodes in compound III-V semiconductors is challenging. Typical multi-quantum-well (MQW) based III-V distributed feedback (DFB) and distributed Bragg reflector (DBR) lasers have linewidths on the order of MHz, due to a variety of factors, including high cavity losses, spontaneous emission coupling into the laser mode, high linewidth enhancement factors, and the onset spatial hole burning (SHB) at high powers [9]. The narrowest demonstrated linewidth in a monolithic DFB laser is 3.6 kHz [10] using a structure designed specifically to minimize the aforementioned effects. Similar issues are present in monolithic DBRs, with the narrowest demonstrated linewidths still exceeding 40 kHz [11–13]. Monolithic quantum dot (QD) lasers show promise for narrow linewidth DFBs. Several QD DFB lasers have demonstrated linewidths <100 kHz [14,15], but so far they have not surpassed the linewidths of the best MQW lasers.

Discrete-mode (DM) lasers are an alternative to DFB and DBR lasers. In a DM laser, refractive index perturbations are introduced along the length of a Fabry-Perot (FP) laser cavity to tune the modal threshold gain spectrum such that only one mode will lase. In most monolithic DM lasers, the facets act as broadband mirrors and slots etched in a rib waveguide produce refractive index perturbations for mode selection. Linewidths on the order of 100 kHz are routine [16], with a minimum linewidth of 2.7 kHz reported in [17]. Such narrow linewidths are possible due to reduced intracavity losses, as compared to DFBs, as well as the spectral filtering provided by the slot pattern, which reduces coupling of light from non-lasing modes into the lasing mode [18,19]. In [20], a slot pattern is used to produce an active DBR front mirror and allows the light

#412839 https://doi.org/10.1364/OE.412839
Journal © 2020 Received 20 Oct 2020; revised 26 Nov 2020; accepted 1 Dec 2020; published 7 Dec 2020

Optics EXPRESS

to be used on-chip, but in later demonstrations [21] the narrowest linewidth in a 12 laser array was around 350 kHz.

Hybrid platforms, which combine the benefits of low-loss passive components with a III-V gain chip, can achieve much narrower linewidths than monolithic platforms. In [22], a hybrid laser with a Lorentzian linewidth of about 1.2 kHz was demonstrated, which was comprised of a grating written on a silica-on-silicon (SiO_2-on-Si) platform coupled to a gain chip. This idea was extended in [23], where a similar device with a grating written in silicon nitride (SiN) achieved a Lorentzian linewidth of about 320 Hz. Hybrid III-V-on-Si platforms combine the functionality of silicon-on-insulator (SOI) with III-V for amplification, without the packaging difficulties associated with actively aligning multiple chips. In [24], a III-V-on-Si DFB laser with an optimized grating geometry achieved a linewidth of 28 kHz. In later work [25], a thicker SiO_2 buffer layer was used between the Si and the III-V, which reduced the cavity losses and allowed the laser to achieve a Lorentzian linewidth of about 1 kHz, but the output power was limited to about 1 mW. A III-V-on-Si DBR laser with a very weak grating was demonstrated in [26] with a linewidth of about 1 kHz and 37 mW of on-chip power, and a similar device with an additional intracavity filter had a linewidth $\leq$500 Hz. Another recent approach for narrow linewidth operation is shown in [27], where a III-V-on-Si amplifier and a low κ SiN mirror are integrated on the same platform, and produced Lorentzian linewidths in the range of 4-6 kHz, but available on-chip power was limited to 0.5 mW.

In this work, we demonstrate O-band hybrid III-V-on-silicon discrete-mode lasers using the Back-Side-on-Buried-Oxide (BSoBOX) laser integration process presented in [28]. The devices were fabricated in a foundry using conventional 193 nm photolithography and required no active alignment steps, complex packaging, or thermal tuning. The lasers can be integrated into more complex SOI based multilayer platforms without adding additional complexity to the III-V integration steps. The DM lasers produced up to 19 mW of on-chip power and have Lorentzian linewidths around 20 kHz, with the best device having a threshold of I_{th} = 35 mA, maximum output power of 17 mW, a minimum Lorentzian linewidth ($I = 5.4 \times I_{th}$) of 18 kHz, and an equipment-limited side mode suppression ratio (SMSR) of at least 60 dB. The design and characterization of the devices are reported and a path toward future device improvement is discussed.

2. Device design

In this section, we provide an overview on the design of the hybrid DM lasers. The general DM laser design procedure starts from a multimode, Fabry-Perot (FP) type laser cavity, and a series of refractive index perturbations along the cavity length are introduced to modify the modal gain to select just one longitudinal mode for oscillation. The impact of a refractive index perturbation on the modal gain spectrum of a FP laser was analyzed in [29]. The theory is expanded in [30], where a perturbative inverse scattering approach to laser cavity design is developed. In the perturbative inverse scattering method, an arbitrary modal threshold gain spectrum is specified in frequency-space, and an inverse design algorithm computes the positions of features within the laser cavity required to replicate the threshold gain spectrum in the device. The ability to arbitrarily tailor the modal gain spectrum provides exceptional freedom in laser design, and many laser designs have been demonstrated on monolithic III-V using this approach, including single mode lasers [29,30], two-color lasers [31,32], and mode locked lasers [33].

First, we designed a FP laser cavity composed of two broadband mirrors and a III-V-on-Si amplifier. A longitudinal cross-section of a DM laser using the BSoBOX laser integration process is shown in Fig. 1(a). The FP laser was nominally identical but lacked the slots etched into the Si rib under the amplifier. A cross-section of the amplifier and its fundamental mode are shown in Fig. 1(b) and (c), respectively. The BSoBOX platform consists of a 6 quantum well (QW) III-V stack bonded to the back side of a 300 nm thick crystalline silicon (c-Si) layer with a 160

Optics EXPRESS

nm thick partial etch layer. A 20 nm SiO_2 spacer acts as a bonding interface between the Si and the III-V. The physical length of the laser cavity was 660 μm, which comprised a 400 μm long amplifier with a 130 μm long transition to the c-Si rib waveguide on both ends.

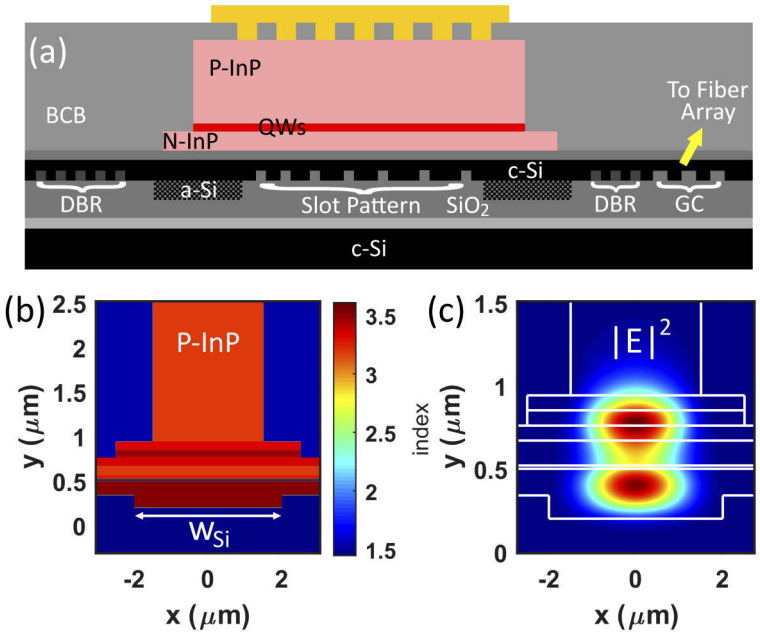

Fig. 1. (a) Longitudinal cross section of a DM laser on the BSoBOX platform. The FP laser is nominally identical, but lacking the slots under the amplifier. (b) Cross-section and (c) Optical mode profile of the amplifier used in the DM lasers.

Optical feedback was provided by front and rear DBR mirrors etched into the c-Si. The DBRs were formed by alternating 400 nm wide and 1200 nm wide Si rib waveguides, producing an index difference of about $\Delta n_{eff} = 0.18$. The DBR period was 214 nm, designed for peak reflection around 1295 nm, and the grating fill factor was 0.5. The rear mirror was 93 periods long (~20 μm) and the front mirror was either 16 or 26 periods (low reflectivity (LR) and high reflectivity (HR) variants, respectively). Simulated reflection spectra of the DBR mirrors are shown in Fig. 2(a). Unlike monolithic DM lasers, where broadband reflectivity is provided by cleaved facets and the modal gain bandwidth is determined by the gain medium, in this work, the modal gain bandwidth is limited by the rear DBR mirror. The simulated bandwidth of the rear mirror, $\Delta\lambda_{DBR}$, is about 36 nm. For a group index around 3.8, the FP laser is then expected to have about 100 longitudinal modes within the rear mirror bandwidth.

To transition between the 400 nm wide Si rib waveguides and the 4 μm wide hybrid waveguide, interlayer transitions were designed following the methodology in [34]. To improve the coupling efficiency between the waveguides, the Si waveguide thickness was increased to 500 nm in the transition region by the local addition of amorphous silicon (a-Si). The addition of the a-Si improved the mode overlap when the N-InP and QW layers are introduced above the Si waveguide. The simulated coupling efficiency of the entire passive transition (i.e. ignoring absorption loss or gain), from the 400 nm wide Si waveguide to the 4 μm wide hybrid waveguide was -0.14 dB at λ = 1295 nm.

To achieve single mode operation, the threshold gain spectrum must be modified such that one longitudinal mode has a considerably lower threshold than all other modes within $\Delta\lambda_{DBR}$. The threshold gain spectrum was modified by the introduction of refractive index perturbations along

Optics EXPRESS

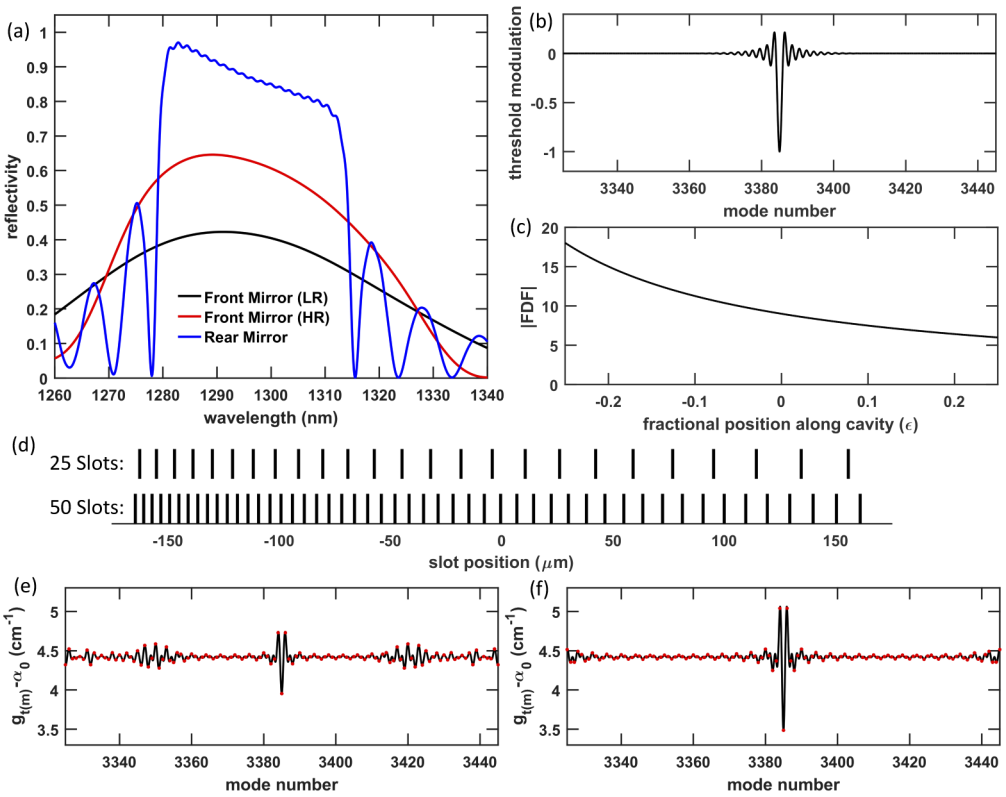

Fig. 2. (a) Simulated reflection spectra of the DBR mirrors. The simulated bandwidth of the rear mirror is about 36 nm. (b) Specified threshold modulation function, which only reduces the threshold gain of mode m_0. (c) Feature density function for the HR designs which was sampled to replicate the threshold modulation function in (b). (d) Slot positions to replicate the threshold modulation function for the DM lasers with HR front mirrors and 25 or 50 slots. The computed threshold gain spectra from the slot patterns in (d) is shown for the 25 slot and 50 slot designs in (e) and (f), respectively.

the amplifier, which were formed by etching quarter-wave (99 nm) slots in the Si rib down to the slab level. The Si rib width in the laser cavity (4 μm) was chosen to maximize the refractive index perturbation due to the introduction of the slots. The simulated drop in refractive index in the slot region was $\Delta n = -0.029$.

To compute the distributions of refractive index perturbations that would produce single mode operation in our devices, we used the perturbative inverse scattering approach developed in [30]. A summary of the technique and the equations required to replicate our designs are included in the Appendix. We designed 4 DM lasers, with identical rear mirrors and either HR or LR front mirrors and 25 or 50 quarter-wave slots for mode selection. In all of our designs, we specified the threshold gain modulation function to be a series of sinc functions, spaced by $a = 50$ modes, modulated by a Gaussian envelope with a full-width-at-half-maximum (FWHM) of about 26 modes. The threshold modulation function is centered at mode $m_0 = 3385$, corresponding to a wavelength of about 1295 nm. The threshold modulation function is shown in Fig. 2(b) and the corresponding feature density function (FDF), which was sampled to replicate the threshold modulation function for the HR designs, is shown in Fig. 2(c). Sampling the FDF with $N = 25$ and $N = 50$ roughly produced the slot patterns in Fig. 2(d).

Optics EXPRESS

To preserve the phase relationship between the slots as the refractive index of the amplifier changes (e.g., due to injected carriers and local heating), the slots should be located in a region of uniform material. We placed the slots below the gain region, between the transitions to the c-Si waveguides. To simplify the design process, the effective index was computed along the length of the laser cavity and the length of each component in the laser cavity L_j was first converted to the amplifier index-normalized length $L_{j,normalized} = L_j\, n_{eff,j}/n_{eff,amplifier}$ and then these lengths were converted to fractional positions along the laser cavity, ϵ, which ranges from -0.5 to 0.5 with the center of the laser cavity at $z = 0$. Working in these new spatial units, the amplifier spans -0.3 to 0.3, accounting for about 60% of the optical path length within the laser cavity. To ensure all slots lie within the amplifier region, the algorithm to compute the location of the slots is bounded by $-0.25 \leq \epsilon \leq 0.25$.

To set the exact slot positions, the rough positions are first tuned to ensure the spacing between slots corresponds to quarter-wave cavities ($L_j = (S + 1/2)(\lambda/n_{eff}), S = 0, 1, 2, \ldots$). Figure 2(e) and (f) show the computed threshold gain spectra $g_{t(m)}$ in our devices with 25 and 50 slots, respectively, computed from the slot positions in (d) after ensuring the quarter-wave condition was met. The computation in (e) and (f) assumes a front mirror reflectivity of 63% and rear mirror reflectivity of 88% at λ = 1295 nm. Lastly, the slot positions were again fine-tuned to account for the small variations in optical path length seen by a single slot due to the presence of other slots, which reduces the amplifier index in that region by Δn.

3. Device characterization

The devices were fabricated on 300 mm SOI wafers following the BSoBOX process flow described in [34]. The devices described here are located side-by-side on the same die. After fabrication, the wafers were diced and a chip was mounted on a temperature controlled measurement stage held at 20 °C. Light was collected from a grating coupler designed to have back reflections <-40 dB. The transmission loss of the gratings, which was measured using test structures on the chip, was about 6.8 dB at λ = 1295 nm.

3.1. LI and spectral properties

Optical output power-current (LI) curves for the 6 devices are shown in Fig. 3. The reported power is the on-chip power emitted from the front mirror of the devices. The transmission loss from the grating couplers has been removed from the data in Fig. 3. Devices without slots are named Fabry-Perot (FP) lasers with either low (L) or high (H) front mirror reflectivity. Discrete mode (DM) lasers are characterized by their front mirror reflectivity (L or H) and the number of slots used for mode selection (25 or 50). The threshold currents, I_{th}, for the devices ranged from 33 mA (FP H) to 49 mA (DM L25). The FP lasers produced the most power, with up to 27 mW and 19 mW of on-chip power emitted front mirror of the low reflectivity and high reflectivity designs, respectively. The maximum output power from the DM lasers ranged from 14 mW (DM H50) to 19 mW (DM L25). The threshold currents and output powers are similar to the DFB lasers fabricated on the same platform in [34]. All 4 DM designs operated single-mode and mode-hop free at drive currents up to at least ~5× threshold. Dips in the LI curves at currents ≥200 mA were due to mode hops. The series resistance of the laser diodes was extracted from the IV curves by fitting the curves with a diode equation. The resistance for all 6 devices was between 6-6.8 Ω.

Comparisons of the emission spectra as a function of the injected current are shown in Fig. 4. The resolution bandwidth (RBW) in the plots was 0.2 nm. The mode hop in DM L50 around 200 mA (Fig. 3) can be identified by the change in spontaneous emission in Fig. 4. A detailed comparison of the spectra from three devices (FP H, DM H25, and DM H50), with a RBW of 0.03 nm, is shown in Fig. 5. Similar trends were observed in the low reflectivity devices. Even below threshold (Fig. 5(a)), the impact of the slots is easily noticeable. The FP modes,

Optics EXPRESS

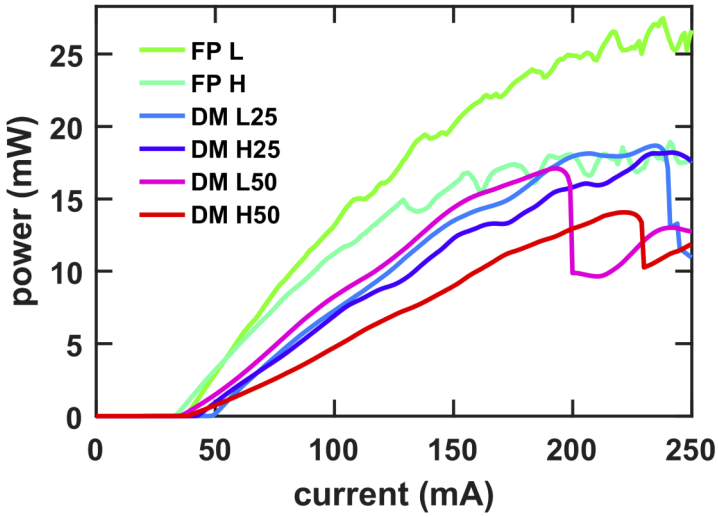

Fig. 3. Light-current (LI) curves for on-chip optical power output of the six devices demonstrated here. Designs with high (H) reflectivity mirrors have lower thresholds but also lower slope efficiency and less maximum output power compared to low (L) reflectivity designs.

which are clearly distinguishable in FP H, have been almost completely suppressed in DM H25 and DM H50. Above threshold (Fig. 5(b)), a single mode quickly begins to dominate the DM spectrum. By ~ 3× I_{th}, all 4 DM lasers were operating with SMSRs ≥57 dB. Around this same current, while the SMSR was still increasing, the side mode nearest the red side of the laser line disappeared below the laser lineshape when the SMSR was in the range of 57-60 dB, due to the limited dynamic range of the optical spectrum analyzer (OSA) at such a narrow offset (~0.35 nm) from the laser line. The SMSRs in DM H25 and DM H50, shown at 180 mA in Fig. 5(c), appear to be 64 dB and 66 dB, but the side mode immediately to the red side of the laser line cannot be resolved.

The bandwidth of the rear DBR was estimated from the spectra of the FP lasers. The nulls in the FP spectra at 1287 nm and 1313 nm correspond to the nulls in the spectrum of the rear DBR mirror in Fig. 2(a). The observed bandwidth, 26 nm, is lower than the simulated value of 36 nm, but some degradation of the mirror performance was expected due to the photolithography and etching of the small features ($\Lambda/2$ = 107 nm) in the DBR mirrors. The group index, n_g, of the laser cavity was computed by Fourier analysis of the FP spectra and was about 3.81 for both the FP lasers. Similar results were obtained for the DM lasers, but with less signal strength due to the suppression of non-lasing modes.

3.2. Optical linewidths

The optical linewidth was measured using delayed self-heterodyne interferometry (DSHI). The interferometer was composed of an isolator, a 3 dB splitter, a polarization controller and phase modulator driven at 500 MHz in one arm and a 25.3 km spool of fiber in the other. The two arms were recombined with a tunable coupler and beat together on a low noise New Focus 1611 photoreceiver, which was AC coupled to an electronic spectrum analyzer. To minimize electronic noise, the lasers were driven by a low noise, ILX Lightwave LDX-3620 laser diode driver in battery operation.

Heterodyne beat signals from the DM lasers at 80 mA, 120 mA, and 160 mA are shown in Fig. 6(a). The resolution bandwidth of the electronic spectrum analyzer was 10 kHz. The

Optics EXPRESS

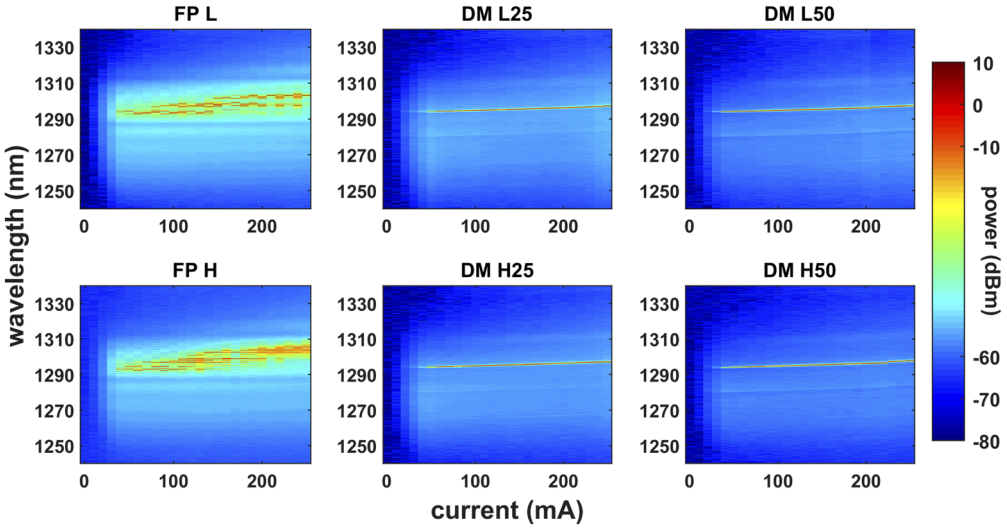

Fig. 4. Optical spectra of the FP and DM lasers. The FP lasers were highly multimode and the DM lasers operated single mode and mode-hop free until currents ≥ 200 mA.

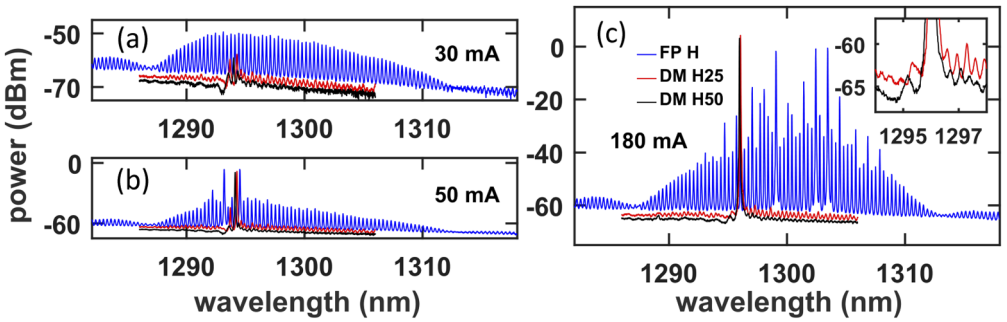

Fig. 5. Optical spectra from high reflectivity devices. The devices are nominally identical aside from the slotted features. The small oscillations in the inset (180 mA) correspond to the suppressed FP modes of the laser cavity.

laser linewidth was determined by fitting the spectra in Fig. 6(a) to a Voigt lineshape. The fits, shown as black traces over the data, were done in log scale to emphasize accurate fitting of the Lorentzian wings of the spectrum. Figure 6(b) shows the linewidth of the Voigt function (Γ_v) as a function of the DC current. Figures 6(c) and (d) show the linewidth of the corresponding Gaussian (Γ_G) and Lorentzian (Γ_L) spectra that must be convolved to produce the traces in (a). In all measurements, the linewidths were dominated by the Gaussian component of the linewidth, which was generally in the 200-300 kHz range and roughly constant with applied current. The Lorentzian component of the linewidth decreased inversely with applied current. The minimum Lorentzian linewidths measured were 23 kHz (DM L25), 39 kHz (DM H25), 18 kHz (DM L50), and 19 kHz (DM H50). In Fig. 6(e), the Lorentzian linewidths in (d) are plotted against $1/P$, where P is the on-chip power from the front mirror of the laser. A single data point at 60 mA (DM L25) had a Lorentzian linewidth ≥ 300 kHz. This data point lies outside the figure axis in Fig. 6(d) and was omitted from the fitting in (e).

Optics EXPRESS

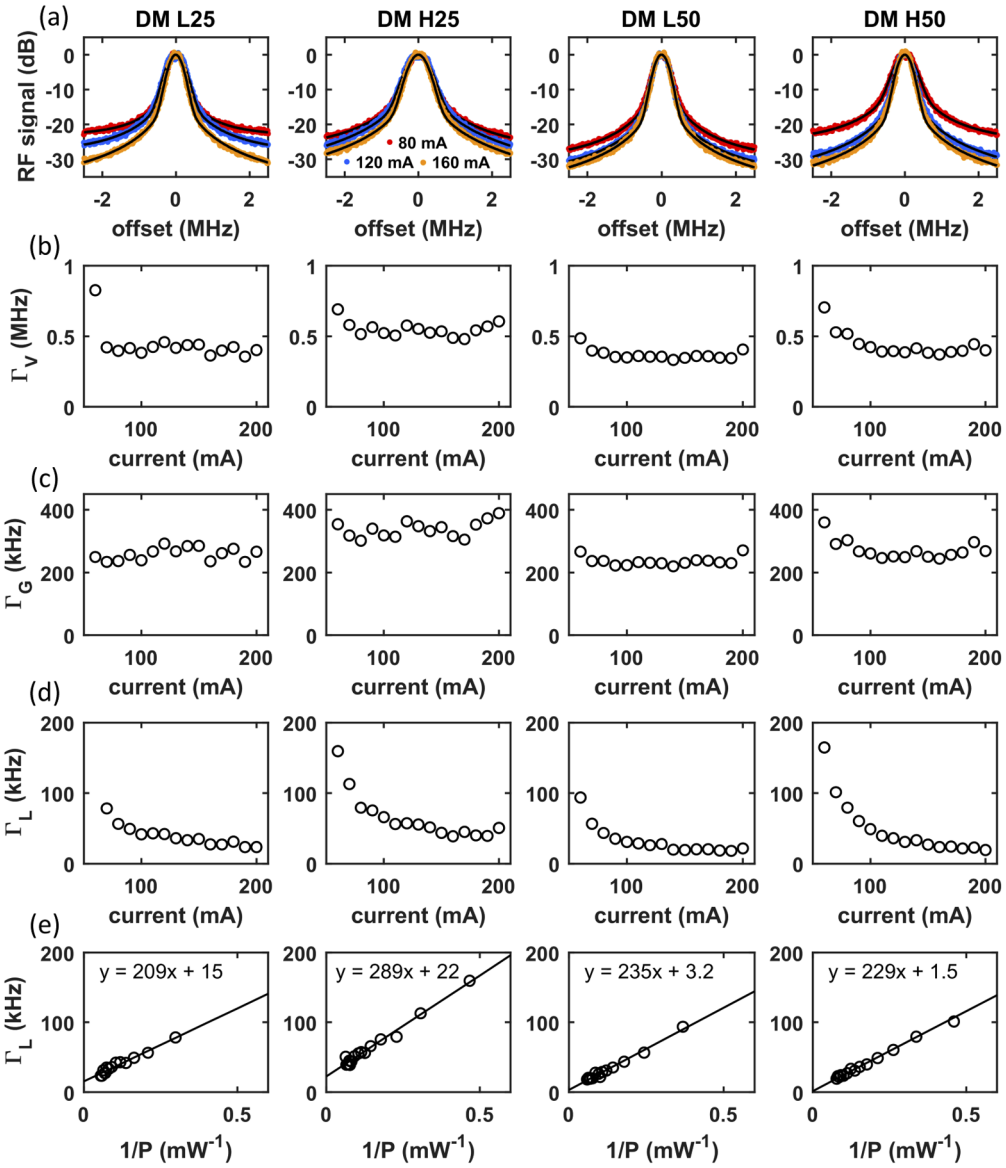

Fig. 6. (a) Heterodyne beat signals from the DM lasers. The black traces are Voigt fits to the spectra. (b) Linewidth of the Voigt functions (Γ_V) extracted from the fits in (a). (c) and (d) show the linewidth of the Gaussian (Γ_G) and Lorentzian (Γ_L) which must be convolved to produce the traces in (a). A single data point (DM L25, 60 mA) had a Lorentzian linewidth $\geq$ 300 kHz and lies far outside the plot axis; this data point was omitted from the fitting in (e). (e) Lorentzian linewidths from (d) plotted against $1/P$. Once the devices are driven sufficiently far above threshold (~60 mA), the Lorentzian linewidth follows the expected linear $1/P$ relationship.

Optics EXPRESS

4. Discussion

A summary of the design parameters and measured characteristics of the FP and DM lasers is shown in Table 1. Compared to the FP lasers, the DM lasers with 25 slots have both higher lasing thresholds and lower output powers. Some reduction in output power was expected and can be attributed to scattering losses due to the slots. The increase in lasing threshold suggests that the scattering losses affect all modes, including m_0, while the reduction in gain threshold only sigificantly affected m_0. Surprisingly, in the devices with 50 slots, where even more scattering would be expected, the threshold currents were lower than those devices with 25 slots. In DM L50, I_{th} has been reduced to below that of the FP laser (I_{th} = 35 mA as compared to 38 mA). Evaluating the trade offs between I_{th}, output power, and the effects of scattering is ongoing.

Table 1. Comparison of Fabry-Perot and Discrete-Mode Lasers

Device	Front	Rear	Slots	I_{th}	P_{max}	$\Gamma_{L,min}$
	Reflectivity	**Reflectivity**		**(mA)**	**(mW)**	**(kHz)**
FP L	0.42	0.88	0	38	27	N/A
DM L25	0.42	0.88	25	48	19	23
DM L50	0.42	0.88	50	35	17	18
FP H	0.63	0.88	0	33	19	N/A
DM H25	0.63	0.88	25	42	18	39
DM H50	0.63	0.88	50	38	14	19

The Gaussian linewidth of the DM lasers remained relatively constant across the current ranges and had similar values across devices, while the Lorentzian component of the linewidth follows the expected linear relationship with $1/P$. The large Gaussian contribution to the linewidth is typically regarded as the result of $1/f$ noise, which is independent of output power and can originate from the measurement setup (e.g., thermal and/or electrical fluctuations) or the device itself, and is more prominent for longer delay lines [35]. To validate our measurement setup, a separate measurement with a reference laser (Agilent 81600B) was performed, which also produced Gaussian linewidths >100 kHz that were relatively constant with output power, while the Lorentzian linewidth followed the expected $1/P$ relationship.

The narrowest Lorentzian linewidth, 18 kHz, was obtained for DM L50, but the result was very similar to DM H50. The linewidths with 50 slots were narrower than 25 slots, suggesting that the mode filtering properties of additional features are more critical to the laser linewidth than the increased cavity losses. The y-intercept of the fits, which gives an extrapolated minimum linewidth as $P \rightarrow \infty$, is about 5 times lower in DM L50 than DM L25, and 15 times lower in DM H50 than DM H25. This is consistent with the theory that the minimum attainable linewidth in practice is likely due to mode coupling effects, and the reduced spontaneous emission in the devices with 50 slots also led to reduced linewidth. The linear fits in 6(e) suggest that linewidths $\leq$10 kHz are attainable if the devices can be kept mode-hop free at higher powers. Compared to our previous work on III-V-on-Si DM lasers [36], the Lorentzian linewidths have been reduced by a factor of about 40. We attribute this to a combination of significant reduced intracavity losses, due to the introduction of a-Si in the transition regions, as well as changing the gain medium from an 8 QW stack to a 6 QW stack with a different QW material composition, designed for higher temperature operation.

Compared to other hybrid III-V-on-Si lasers, our hybrid DM lasers offer an alternative approach toward narrow linewidth lasers that focuses on ease of integration. Compared to the extended DBR laser in [26], the DM lasers have broader linewidths at lower output powers (about 20 kHz at about 20 mW vs. 1 kHz at 40 mW). However, the DM lasers do not require long and weak gratings, so DM lasers are more compact in size (cavity length of 600 μm vs. >15 mm) and they

Optics EXPRESS

can be operated without thermal tuning. Our demonstration also did not require an additional SiN layer to improve the linewidth, as in [27]. Compared to the high-Q photonic crystal DFB design in [24], our DM lasers produce similar linewidths and output power. Compared to the later work in [25], our DM lasers exhibited Lorenztian linewidths that are about 10× broader but with >4× higher output power. However, unlike high-Q photonic crystal designs, our lasers do not require electron-beam lithography to define the gratings.

The performance of the DM laser can be improved in future fabrication iterations. Optimizing the rear mirror to have near 100% reflectivity at the laser wavelength would significantly increase output power. Previous work [36] with nominally identical DBR mirrors to those used in DM H50 and DM H25 showed only 55% of the power emitted from the laser was emitting from the front mirror, suggesting that the usable on-chip power could be nearly doubled with improved mirror design. Replacing the MQW amplifier with a QD based amplifier would reduce the laser linewidth, due to a reduction in the linewidth enhancement factor. Lastly, the inverse scattering algorithm is a powerful, generic tool for inverse design of arbitrary threshold gain spectra. Although this work follows the analytic techniques first described in [29], a numerical exploration and optimization of the parameter space in Eq. (3) may find slot distributions with even greater mode selectivity, further improving SMSR and linewidth.

5. Conclusion

In summary, we have demonstrated O-band III-V-on-Si discrete mode lasers fabricated using the BSoBOX laser integration process. To the best of our knowledge, this is the first demonstration of discrete mode lasers in a hybrid III-V-on-Si platform. The best device produced 17 mW of output power, with a Lorentzian linewidth of 18 kHz and an OSA-limited SMSR of at least 60 dB. Future work will focus on optimizing the devices to produce higher output powers and narrower linewidths, as well as their integration in more complex photonic circuits.

Appendix

This appendix summarizes the results of numerous derivations and explanations in [29–32,37] which developed the perturbative inverse scattering approach and the equations required to replicate these designs. In the inverse scattering approach, a threshold gain spectrum is defined in frequency-space and the Fourier transform defines a feature density function, which can be sampled to produce a device with the corresponding threshold gain spectrum. Detailed explanations of all parameters and full derivations can be found in the original texts.

The gain threshold, $g^{(0)}_{t(m)}$, for the m^{th} ($m = m_0 + \Delta m$) longitudinal mode of a simple FP laser is given by

$$g^{(0)}_{t(m)} = \alpha_0 - \frac{1}{L}\ln(r_1 r_2), \tag{1}$$

where α_0 is the propagation loss due to absorption and scattering, L is the length of the laser cavity, and r_1 and r_2 are the mirror reflection coefficients. To simplify the analysis, the reflection coefficients r_1 and r_2 are treated as real and the gain threshold $g^{(0)}_{t(m)}$=$g^{(0)}_t$ is treated as constant over the mirror bandwidth $\Delta\lambda_{DBR}$. Assuming quarter-wave perturbations at the wavelength of mode m_0, which maximize the impact of the perturbation, introducing N refractive index perturbations to the laser cavity causes a change in the modal gain spectrum (to first order) of the form

$$g_{t(m)} = g^{(0)}_t + \frac{\Delta n}{n_{eff}} g^{(1)}_m, \tag{2}$$

where Δn is the refractive index perturbation and

$$g^{(1)}_m = \frac{1}{L\sqrt{r_1 r_2}} \cos(m_0\pi)\cos(\Delta m\pi) \sum_{j=1}^{N} A(\epsilon_j)\sin(2\pi\epsilon_j m_0)\cos(2\pi\epsilon_j \Delta m). \tag{3}$$

Optics EXPRESS

In Eq. (3), ϵ_j is the fractional position along the laser cavity at the center of the j^{th} slot and spans from -0.5 to 0.5, and

$$A(\epsilon_j) = r_1 \exp(\epsilon_j L g_t^{(0)}) - r_2 \exp(-\epsilon_j L g_t^{(0)}). \tag{4}$$

Eq. (3) specifies the change in threshold gain for the m^{th} mode and depends on the difference in round-trip gain on each side of the slot [32].

To produce a single-mode laser, the threshold gain spectrum must be modified such that a desired mode m_0 has a lower gain threshold than modes $m \neq m_0$ within $\Delta\lambda_{DBR}$. One example of a suitable threshold modulation function is the function sinc(Δm), which is 1 for $\Delta m = 0$ and 0 for $\Delta m \neq 0$. The threshold modulation function can be defined as a series of sinc functions modulated by a Gaussian

$$g_{t(\Delta m)}^{(0)} - g_t^{(0)} \propto \exp\left[-\pi\tau^2(\Delta m)^2\right] \sum_{n=-\infty}^{\infty} \mathrm{sinc}(\Delta m - na), \tag{5}$$

where a defines the number of modes separating each sinc function and τ specifies how rapidly the Gaussian envelope decays. The threshold modulation is a function chosen both for its useful spectral properties, as well as having the simple Fourier transform

$$\Gamma(\epsilon) = \sum_{n=-\infty}^{\infty} \exp\left[-\frac{\pi}{\tau^2}(\epsilon - n/a)^2\right], \tag{6}$$

which can be sampled to produce a slot distribution. To account for the fact that the magnitude of the threshold gain modulation depends on the position of the slot within the laser cavity (through $A(\epsilon)$), the feature density function is defined as the product of $A(\epsilon)^{-1}$ with $\Gamma(\epsilon)$. The positions of the slots are then computed by solving the equation

$$C \sum_{j=1}^{N} \int_{\epsilon_{min}}^{\epsilon_j} [A(\epsilon)]^{-1}\Gamma(\epsilon)d\epsilon = j - 1/2, \tag{7}$$

where

$$C = \int_{\epsilon_{min}}^{\epsilon_{max}} [A(\epsilon)]^{-1}\Gamma(\epsilon)d\epsilon \tag{8}$$

is a normalization constant.

Acknowledgment

T. T., J. C. C. M., and J. K. S. P. are grateful for the funding support from the Natural Sciences and Engineering Research Council of Canada (NSERC). SCINTIL Photonics thanks la Banque Publique d'Investissement for its support through the I-LAB2018 contest.

Disclosures

The authors declare no conflicts of interest.

References

1. K. Kikuchi, "Fundamentals of coherent optical fiber communications," J. Lightwave Technol. **34**(1), 157–179 (2016).
2. S. L. Olsson, J. Cho, S. Chandrasekhar, X. Chen, P. J. Winzer, and S. Makovejs, "Probabilistically shaped PDM 4096-QAM transmission over up to 200 km of fiber using standard intradyne detection," Opt. Express **26**(4), 4522–4530 (2018).

Optics EXPRESS

3. K. Zou, Z. Zhang, P. Liao, H. Wang, Y. Cao, A. Almaiman, A. Fallahpour, F. Alishahi, N. Satyan, G. Rakuljic, M. Tur, A. Yariv, and A. E. Willner, "Higher-order QAM data transmission using a high-coherence hybrid Si/III–V semiconductor laser," Opt. Lett. **45**(6), 1499–1502 (2020).
4. D. T. Spencer, T. Drake, T. C. Briles, J. Stone, L. C. Sinclair, C. Fredrick, Q. Li, D. Westly, B. R. Ilic, A. Bluestone, N. Volet, T. Komljenovic, L. Chang, S. H. Lee, D. Y. Oh, M.-G. Suh, K. Y. Yang, M. H. P. Pfeiffer, T. J. Kippenberg, E. Norberg, L. Theogarajan, K. Vahala, N. R. Newbury, K. Srinivasan, J. E. Bowers, S. A. Diddams, and S. B. Papp, "An optical-frequency synthesizer using integrated photonics," Nature **557**(7703), 81–85 (2018).
5. D. Marpaung, J. Yao, and J. Capmany, "Integrated microwave photonics," Nat. Photonics **13**(2), 80–90 (2019).
6. J. Chen, Q. Liu, X. Fan, and Z. He, "Ultrahigh resolution optical fiber strain sensor using dual Pound–Drever–Hall feedback loops," Opt. Lett. **41**(5), 1066–1069 (2016).
7. Y.-H. Lai, M.-G. Suh, Y.-K. Lu, B. Shen, Q.-F. Yang, H. Wang, J. Li, S. H. Lee, K. Y. Yang, and K. Vahala, "Earth rotation measured by a chip-scale ring laser gyroscope," Nat. Photonics **14**(6), 345–349 (2020).
8. E. Dale, W. Liang, D. Eliyahu, A. A. Savchenkov, V. S. Ilchenko, A. B. Matsko, D. Seidel, and L. Maleki, "Ultra-narrow line tunable semiconductor lasers for coherent LIDAR applications," in *Imaging and Applied Optics 2014* (Optical Society of America, 2014), p. JTu2C.3.
9. M. Okai, M. Suzuki, T. Taniwatari, and N. Chinone, "Corrugation-pitch-modulated distributed feedback lasers with ultranarrow spectral linewidth," Jpn. J. Appl. Phys. **33**(Part 1, No. 5A), 2563–2570 (1994).
10. M. Okai, M. Suzuki, and T. Taniwatari, "Strained multiquantum-well corrugation-pitch-modulated distributed feedback laser with ultranarrow (3.6 kHz) spectral linewidth," Electron. Lett. **29**(19), 1696–1697 (1993).
11. S. C. Davies, R. A. Griffin, A. J. Ward, N. D. Whitbread, I. Davies, L. Langley, S. Fourte, J. Mo, Y. Xu, and A. Carter, "Narrow linewidth, high power, high operating temperature digital supermode distributed Bragg reflector laser," in *39th European Conference and Exhibition on Optical Communication (ECOC 2013)* (Institution of Engineering and Technology, 2013), pp. 691–693
12. M. C. Larson, A. Bhardwaj, W. Xiong, Y. Feng, X. D. Huang, K. P. Petrov, M. Moewe, H. Y. Ji, A. Semakov, C. W. Lv, S. Kutty, A. Patwardhan, N. Liu, Z. M. Li, Y. J. Bao, Z. H. Shen, S. Bajwa, F. H. Zhou, and P. C. Koh, "Narrow linewidth sampled-grating distributed Bragg reflector laser with enhanced side-mode suppression," in *Optical Fiber Communication Conference* (Optical Society of America, 2015), p. M2D.1.
13. S. Andreou, K. A. Williams, and E. A. J. M. Bente, "Monolithically integrated InP-based DBR lasers with an intra-cavity ring resonator," Opt. Express **27**(19), 26281–26294 (2019).
14. J. Duan, H. Huang, Z. Lu, P. Poole, C. Wang, and F. Grillot, "Narrow spectral linewidth in InAs/InP quantum dot distributed feedback lasers," Appl. Phys. Lett. **112**(12), 121102 (2018).
15. T. Septon, S. Gosh, A. Becker, V. Sichkovskyi, F. Schnabel, A. Rippien, J. P. Reithmaier, and G. Eisenstein, "Narrow linewidth InAs/InP quantum dot DFB laser," in *Optical Fiber Communications Conference* (Optical Society of America, 2019), p. W3A.8.
16. B. Kelly, R. Phelan, D. Jones, C. Herbert, J. O'Carroll, M. Rensing, J. Wendelboe, C. B. Watts, A. Kaszubowska-Anandarajah, P. Perry, C. Guignard, L. P. Barry, and J. O'Gorman, "Discrete mode laser diodes with very narrow linewidth emission," Electron. Lett. **43**(23), 1282–00 (2007).
17. R. Phelan, B. Kelly, D. Jones, C. Herbert, J. O'Carroll, M. Rensing, B. Cai, A. Kaszubowska-Anandarajah, P. Perry, J. Stopford, P. Anandarajah, L. P. Barry, and J. O'Gorman, "Discrete mode laser diodes with ultra narrow linewidth emission < 3kHz," in *Optical Fiber Communication Conference/National Fiber Optic Engineers Conference* (Optical Society of America, 2008), p. OThK5.
18. W. Elsasser and E. Gobel, "Multimode effects in the spectral linewidth of semiconductor lasers," IEEE J. Quantum Electron. **21**(6), 687–692 (1985).
19. C. Herbert, D. Jones, A. Kaszubowska-Anandarajah, B. Kelly, M. Rensing, J. O'Carroll, R. Phelan, P. Anandarajah, P. Perry, L. P. Barry, and J. O'Gorman, "Discrete mode lasers for communication applications," IET Optoelectron. **3**(1), 1–17 (2009).
20. Q. Lu, W. Guo, M. Nawrocka, A. Abdullaev, C. Daunt, J. O'Callaghan, M. Lynch, V. Weldon, F. Peters, and J. F. Donegan, "Single mode lasers based on slots suitable for photonic integration," Opt. Express **19**(26), B140–B145 (2011).
21. A. Abdullaev, Q. Lu, W. Guo, M. J. Wallace, M. Nawrocka, F. Bello, A. Benson, J. O'Callaghan, and J. F. Donegan, "Improved performance of tunable single-mode laser array based on high-order slotted surface grating," Opt. Express **23**(9), 12072–12078 (2015).
22. L. Stolpner, "Planar External Cavity Low Noise Narrow Linewidth Lasers," presented at the *7th Annual Photonic Doppler Velocimetry (PDV) Workshop*, Albuquerque, New Mexico, October 2011.
23. C. Xiang, P. A. Morton, and J. E. Bowers, "Ultra-narrow linewidth laser based on a semiconductor gain chip and extended Si_3N_4 Bragg grating," Opt. Lett. **44**(15), 3825–3828 (2019).
24. H. Wang, D. Kim, M. Harfouche, C. T. Santis, N. Satyan, G. Rakuljic, and A. Yariv, "Narrow-linewidth oxide-confined heterogeneously integrated Si/III-V semiconductor lasers," IEEE Photonics Technol. Lett. **29**(24), 2199–2202 (2017).
25. C. T. Santis, Y. Vilenchik, N. Satyan, G. Rakuljic, and A. Yariv, "Quantum control of phase fluctuations in semiconductor lasers," Proc. Natl. Acad. Sci. **115**(34), E7896–E7904 (2018).
26. D. Huang, M. A. Tran, J. Guo, J. Peters, T. Komljenovic, A. Malik, P. A. Morton, and J. E. Bowers, "High-power sub-kHz linewidth lasers fully integrated on silicon," Optica **6**(6), 745–752 (2019).

Optics EXPRESS

27. C. Xiang, W. Jin, J. Guo, J. D. Peters, M. J. Kennedy, J. Selvidge, P. A. Morton, and J. E. Bowers, "Narrow-linewidth III-V/Si/Si_3N_4 laser using multilayer heterogeneous integration," Optica **7**(1), 20–21 (2020).
28. S. Menezo, T. Thiessen, G. El-Zammar, J. Mak, J. Da Fonseca, P. Brianceau, B. Szelag, C. Jany, and J. K. S. Poon, "Back-side-on-BOX heterogeneous laser integration for fully integrated photonic circuits on silicon," in *45th European Conference on Optical Communication (ECOC 2019)* (Institution of Engineering and Technology, 2019) pp. 1–3.
29. S. O'Brien and E. P. O'Reilly, "Theory of improved spectral purity in index patterned Fabry-Parot lasers," Appl. Phys. Lett. **86**(20), 201101 (2005).
30. S. O'Brien, A. Amann, R. Fehse, S. Osborne, E. P. O'Reilly, and J. M. Rondinelli, "Spectral manipulation in Fabry-Perot lasers: perturbative inverse scattering approach," J. Opt. Soc. Am. B **23**(6), 1046–1056 (2006).
31. S. O'Brien, S. Osborne, K. Buckley, R. Fehse, A. Amann, E. P. O'Reilly, L. P. Barry, P. Anandarajah, J. Patchell, and J. O'Gorman, "Inverse scattering approach to multiwavelength Fabry-Parot laser design," Phys. Rev. A **74**(6), 063814 (2006).
32. S. Osborne, S. O'Brien, K. Buckley, R. Fehse, A. Amann, J. Patchell, B. Kelly, D. R. Jones, J. O'Gorman, and E. P. O'Reilly, "Design of single-mode and two-color Fabry-Parot lasers with patterned refractive index," IEEE J. Sel. Top. Quantum Electron. **13**(5), 1157–1163 (2007).
33. D. Bitauld, S. Osborne, and S. O'Brien, "Passive harmonic mode locking by mode selection in Fabry-Parot diode lasers with patterned effective index," Opt. Lett. **35**(13), 2200–2202 (2010).
34. T. Thiessen, J. C. C. Mak, J. D. Fonseca, K. Ribaud, C. Jany, J. K. S. Poon, and S. Menezo, "Back-side-on-BOX heterogeneously integrated III-V-on-silicon O-band distributed feedback lasers," J. Lightwave Technol. **38**(11), 3000–3006 (2020).
35. L. B. Mercer, "1/f frequency noise effects on self-heterodyne linewidth measurements," J. Lightwave Technol. **9**(4), 485–493 (1991).
36. T. Thiessen, J. Da Fonseca, J. C. C. Mak, G. E. Zammar, C. Jany, B. Szelag, J. K. S. Poon, and S. Menezo, "Backside-processed III-V-on-silicon discrete mode laser," in *Conference on Lasers and Electro-Optics* (Optical Society of America, 2019), p. JTh5A.1.
37. S. O'Brien, F. Smyth, K. Shi, J. O'Carroll, P. M. Anandarajah, D. Bitauld, S. Osborne, R. Phelan, B. Kelly, J. O'Gorman, F. H. Peters, B. Roycroft, B. Corbett, and L. P. Barry, "Design, characterization, and applications of index-patterned Fabry-Parot lasers," IEEE J. Sel. Top. Quantum Electron. **17**(6), 1621–1631 (2011).